

Lattice Energetics and Correlation-Driven Metal-Insulator Transitions: the Case of Ca_2RuO_4

Qiang Han¹ and Andrew Millis^{1,2}

¹*Department of Physics, Columbia University, New York, New York 10027*

²*The Center for Computational Quantum Physics, The Flatiron Institute, New York, NY 10010*

(Dated: January 22, 2018)

Many materials exhibit metal-insulator transitions that are driven by electron correlation effects but also involve structural changes. This paper uses density functional, dynamical mean field and Landau-theory methods to elucidate the interplay of electronic and structural energetics in Ca_2RuO_4 . We find that the change in lattice energies across the metal-insulator transition is comparable to the change in electronic energies. Important consequences are the strongly first order nature of the transition, a sensitive dependence on pressure, and that imposition of geometrical constraints (for example via epitaxial growth on a substrate) can change the lattice energetics enough to eliminate the metal-insulator transition entirely. A comparison to recent data is presented.

PACS numbers: 71.27.+a, 75.50.Cc, 72.15.Eb

Many materials exhibit metal-insulator transitions of the "Mott" type, primarily driven by electron-electron interactions¹ but also involving changes in atomic positions. For example, the insulating phases of the rare earth titanates and vanadates are believed to be stabilized by a GdFeO_3 -type octahedral rotation,^{2,3} while in the rare earth manganites the insulating phase is associated with an approximately volume-preserving even-parity octahedral distortion⁴⁻⁶. In perovskite nickelates the metal-insulator transition involves a two sub-lattice disproportionation of the Ni-O bond length.⁷⁻¹⁰

An understanding of the role of the lattice energetics in the metal-insulator transition has been lacking. Mott argued that the change in electronic screening across the metal-insulator transition would change the bulk modulus, causing a change in volume between metallic and insulating phases and driving an otherwise second order transition to first order.¹¹ However, because most of the screening is associated with high energy ($\sim 10 - 20\text{eV}$) excitations,¹² the change in bulk modulus across the metal insulator transition is typically small. In typical modern correlated electron calculations¹³ the metal-insulator phase diagram is explored as a function of lattice coordinates without reference to whether the lattice coordinates in question correspond to any equilibrium crystal structure: forces and energy minimization are only now beginning to become available¹⁴⁻¹⁶ and the contribution of the lattice distortions to the energetics of the metal insulator transition is only now beginning to receive attention.

This paper addresses the roles of lattice energetics and strain coupling in Mott transitions. We focus on Ca_2RuO_4 which exhibits a correlation-driven metal-insulator transition¹⁷ accompanied by a large amplitude, symmetry preserving lattice distortion^{18,19}. We introduce a free energy functional and use a combination of empirical arguments, density functional theory (DFT) and dynamical mean field (DMFT) calculations to fix parameters. We define a lattice stabilization energy and show that in Ca_2RuO_4 it is comparable to the elec-

tronic contribution. The theory accounts for the observed strain and pressure dependence of the metal-insulator transition²⁰⁻²³ and shows that epitaxial constraints can entirely eliminate the transition.

The degrees of freedom of the theory are a state variable a distinguishing the electronic phase (metallic or insulating) and a set of lattice variables (ionic positions and strains) which we define in terms of changes with respect to a reference configuration Q^* and assemble into a vector $\delta\vec{Q}$. We assume that the lattice free energy is harmonic in $\delta\vec{Q}$, with a force constant matrix \mathbf{K} that is independent of the electronic state (we will see that this assumption is justified for Ca_2RuO_4) and an electronic state-dependent linear term \vec{F}^a that specifies the force exerted by the electronic state on the lattice. The free energy is then

$$F^a(\delta\vec{Q}) = F_0^a + \vec{F}^a \cdot \delta\vec{Q} + \frac{1}{2} \delta\vec{Q}^T \cdot \mathbf{K} \cdot \delta\vec{Q} \quad (1)$$

Here F_0^a is the electronic free energy in state a at $\delta\vec{Q} = 0$; it has a temperature dependence (not notated) that represents the electronic physics of the transition. In Eq. 1 we haven't explicitly notated the important fact that each electronic state is only stable for a certain region of $\delta\vec{Q}$. Minimizing Eq. 1 with respect to the lattice degrees of freedom gives

$$\delta\vec{Q} = -\mathbf{K}^{-1} \cdot \vec{F}^a \quad \text{and} \quad F_{min} = F_0^a - \frac{1}{2} \vec{F}^a{}^T \cdot \mathbf{K}^{-1} \cdot \vec{F}^a \quad (2)$$

Eq. 2 shows that if the lattice is allowed to relax the phase a gains the stabilization energy

$$E_{stabil}^a = -\frac{1}{2} \vec{F}^a{}^T \cdot \mathbf{K}^{-1} \cdot \vec{F}^a \quad (3)$$

We now apply these generic considerations to Ca_2RuO_4 . Ca_2RuO_4 crystallizes in a Pbca -symmetry structure with four formula units in each unit cell. The basic structural unit is the Ru-O_6 octahedron; these form corner-shared planes separated from adjacent Ru planes

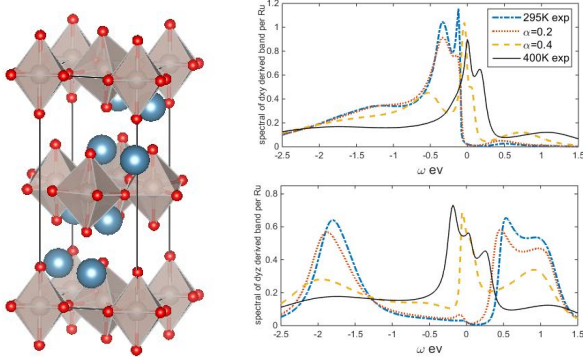


FIG. 1. Left panel: Representation of the unit cell of Ca_2RuO_4 . Gray balls are ruthenium atoms, red balls oxygen atoms and blue balls calcium atoms. Right panel: Orbitaly resolved densities of states for structures interpolating between experimental 295K and 400K structures. Upper panel: xy orbital; lower panel yz orbital (xz is very similar). $\alpha = 0$ is the 295K structure; $\alpha = 1$ is the 400K structure; $\alpha = 0.4$ is in the metallic phase but very close to the transition point; the $\alpha = 0.6, 0.8$ spectra are very similar to the 400K spectra and are omitted for clarity.

by spacer layers involving Ca atoms; see the left panel of Figure 1. The Pbc structure is derived from the ideal tetragonal $n = 1$ Ruddlesden-Popper structure by rotations of the Ru-O_6 octahedra about the apical $\text{Ru-O}(2)$ bond, tilts of this axis with respect to the $\text{Ru-O}(1)$ plane, as well as an additional distortion that makes the two in-plane Ru-O bond lengths slightly different. We distinguish the four in-plane ($\text{Ru-O}(1)$) and two apical ($\text{Ru-O}(2)$) Ru-O bonds. The $\text{Ru-O}(2)$ and average (over the two in-plane directions) $\text{Ru-O}(1)$ bond lengths are the crucial variables in the electronic energetics. Their values across the metal-insulator transition are presented in Table I. The bond lengths continue to evolve as temperature is further lowered though the insulating phase^{18,19}.

The corner-shared structure implies that if the rotation angles remain fixed, the $\text{Ru-O}(1)$ bond-lengths predicts the average in-plane lattice parameter. Density functional calculations (see supplementary material) and experiments show that changes in the rotation angles are negligible for reasonable strains, so the Ru-Ru and $\text{Ru-O}(1)$ distances are not independent variables. On the other hand, the c-axis stacking of the Ruddlesden-Popper structure means that at fixed c-axis lattice constant changes in the $\text{Ru-O}(2)$ bond length can be accommodated by a buckling of the Ca-O planes.

We will be interested here in structures in which the c-axis lattice parameter is relaxed for given values of the octahedral bond-lengths. Thus the lattice degrees of freedom that need to be retained in our theory are the average $\text{Ru-O}(1)$ and $\text{Ru-O}(2)$ distances. We parametrize the Ru-O bond lengths in terms of changes $\delta s^o = \frac{1}{\sqrt{2}}(\delta x + \delta y)$, δz with respect to a reference state, which we take to be the 400K metallic state, and we ex-

press these in terms of the octahedral coordinates

$$\delta Q_0 = \frac{1}{\sqrt{3}}(\delta z + \sqrt{2}\delta s^o) \quad \delta Q_3 = \frac{1}{\sqrt{6}}(2\delta z - \sqrt{2}\delta s^o) \quad (4)$$

which we assemble into the vector $\delta \vec{Q} = (\delta Q_3, \delta Q_0)$. The \mathbf{K} in Eq. 1 is then a 2×2 matrix derived from the dependence of the energies on δQ_3 and δQ_0 , with the out of plane lattice constant relaxed for each value of $\delta \vec{Q}$. We used density functional plus U (DFT+U) calculations and observed phonon frequencies (which give energetics of Ru-O bond length changes without lattice relaxation) to estimate the entries of \mathbf{K} (see supplementary material for details), finding $K_{33} = 17.7$, $K_{03} = 7.6$, $K_{00} = 46.2$ $\text{eV}/\text{\AA}^2$ per formula unit. The observation²⁴⁻²⁶ that the changes in optical phonon frequencies across the transition, are about 2% justifies the harmonic approximation and the independence of \mathbf{K} on the electronic phase.

TABLE I. Experimentally determined apical ($\text{Ru-O}(2)$) and average in-plane ($\text{Ru-O}(1)$) bond lengths and octahedral distortions (Eq. 4) in \AA at $T=295$ K [18] and 400 K [19], and occupancy (per spin per atom) of xy, yz and zx derived bands from DMFT calculation (n_{xy}) using the experimentally determined lattice structures for the listed temperatures.

	$\text{RuO}(2)$	$\text{RuO}(1)$	δQ_0	δQ_3	n_{xy}	$\bar{n}_{yz/zx}$
400 K	2.042	1.95	0.0	0.0	0.671	0.665
295 K	1.995	1.99	0.0196	-0.069	0.982	0.5075

We now turn to the electronic degrees of freedom. The relevant frontier electronic states are t_{2g} -derived Ru-4d oxygen 2p antibonding states which we refer to as Ru d states, following standard practice²⁷⁻³¹. The t_{2g} -derived bands are sufficiently well separated from the other bands that we may focus our treatment of the correlation problem on them, treating the other bands as inert²⁹⁻³¹. The tetragonal symmetry splits the t_{2g} -derived triplet into a singlet (d_{xy}) and a doublet (d_{xz} and d_{yz}). The octahedral rotations and other distortions (angles $\sim 10^\circ$) provide small additional rearrangements of the level structure (in particular lifting the xz/yz degeneracy), but as long as the orbitals are defined with respect to the local octahedral symmetry axes, the deviations from the perfectly tetragonal structure do not significantly affect the on-site level splitting, basic energetics or assignment of orbital character. Spin-orbit effects (coupling $\lambda_{SOC} \approx 0.1\text{eV}$) are important for lower T magnetic properties of the insulating state^{26,32,33} but the spin-orbit energy scales are small enough that spin orbit coupling is not relevant to the physics we consider here.

We have performed DFT and DFT+DMFT calculations (see supplementary information for details). We find, in agreement with previously work²⁹ that use of the experimentally determined 400K structure produces a moderately correlated metallic solution while use of the 295K structure produces a Mott insulator. The metallic state is characterized by an approximately equal occupation of the three t_{2g} orbitals. The nearly equal occu-

pancies, which are not enforced by any symmetry, arise because in the metallic phase the interactions strongly scatter the electrons among orbitals (this is also why, despite the density of state differences at the DFT level, the many-body densities of states look very similar in the metallic phase). The insulating state is orbitally disproportionated, with an essentially fully filled xy band and half filled, much narrower, xz/yz bands of the form expected for a Mott insulator with upper and lower Hubbard bands separated by a gap. The calculated orbital occupancies for the two phases are given in Table I.

We expect that changing the lattice structure affects the transition in two ways: decreasing the octahedral distortion δQ_3 lowers the on-site energy of the xy orbital relative to that of the xz/yz orbitals, favoring the insulating phase, while decreasing the in-plane Ru-O bond length (and, interestingly, also decreasing the Ru-O(2) bond length) increases the bandwidth, favoring the metallic phase. The right-hand panels of Fig. 1 present the orbitally resolved densities of states obtained from DFT+DMFT calculations performed for a series of structures interpolating between the T=295K ($\alpha = 0$) and T=400K ($\alpha = 1$) structures. We have also performed calculations in which the Ru-O(2) (apical) bond length is gradually varied with other structural parameters remaining fixed; the results are very similar. The metallic states $\alpha = 1$, $\alpha = 0.8$, 0.6 (not shown) and $\alpha = 0.4$ reveal a gradual evolution of the bands, with a shift of carriers

from the xz/yz orbitals to the xy orbitals ((n_{xy}, n_{xz}, n_{yz}) changes from $\approx (4/3, 4/3, 4/3)$ to $\approx (5/3, 7/6, 7/6)$ as α changes from 1 to 0.4 and then a first order metal-insulator transition for α just slightly smaller than 0.4 to a state with α -independent occupancies (2, 1, 1). The two insulating phase structures $\alpha = 0.2$ and $\alpha = 0$ reveal very similar densities of states with an approximately 0.1eV shift upward of the xz/yz band relative to the xy band as α changes from 0.2 to 0. Although the transition is first order we have not observed coexistence of metal and insulator phases at any of the lattice configurations we have studied.

Fig. 2 plots the DFT+DMFT energy of the correlated bands for interpolated and c-axis stretched structures against a linear function of octahedral parameters (Eq. 4). The particular linear combination of structural parameters is chosen so that the data from the two different families of structures (which change the bandwidth and octahedral distortion in different proportions) collapses. We emphasize that the insulating (metallic) state is only stable for $\delta Q_3 - \lambda_0 \delta Q_0 < (>) \delta Q_c \approx 0.04\text{\AA}$ (we expect Q_c depends on U, J). And apart from some rounding in the immediate vicinity of the transition, the energy is the same linear function of the structural parameters, with a break in slope across the transition. The choice of variables that provides the data collapse in Fig. 2 fixes the force, that is the break in slope as $\mathcal{F}_3^I = 2.8\text{ ev/\AA}$ and $\mathcal{F}_0^I = -\lambda_0 \mathcal{F}_3^I = -1.3\text{ ev/\AA}$. Here we change the sign of \mathcal{F}_3 since we choose the 400K metal phase as origin of distortions. From the approximately linear evolution of the Ru-O(1) bond length observed in experiments between 110K to 295K^{18,19}, and using the elastic matrix \mathbf{K} we estimate the required force term as

$$\begin{aligned}\mathcal{F}_3^{exp}(T) &= -\mathbf{K}\delta\vec{Q}^{exp}(T) \approx 1.93 - 0.0047(T - 110\text{K}) \\ \mathcal{F}_0^{exp} &\approx -0.35\mathcal{F}_3^{exp}(T)\end{aligned}\quad (5)$$

Thus the DMFT force is about 50% larger than the experiment at the Neel temperature and even larger at room temperature indicating there is a significant entropy effect not present in the DMFT calculation. An estimate of the curvature $\partial^2 E / \partial \delta Q^2$ in each phase is difficult to obtain from these data but the values we obtain are small enough that even given the uncertainties we believe the effect of the metal-insulator transition on \mathbf{K} may be neglected (see supplementary material).

In Fig. 3 we plot the free energy landscape at different temperatures in the plane of Ru-O bond length coordinates $\delta x = \frac{1}{\sqrt{3}}\delta Q_0 - \frac{1}{\sqrt{6}}\delta Q_3$ and $\delta z = \frac{1}{\sqrt{3}}\delta Q_0 + \frac{\sqrt{6}}{3}\delta Q_3$, using force terms estimated in eq 5. We chose the metallic state at $T > T_{M-I}$ as the reference. At high temperature, there is no global minimum in the insulating phase. As $T \leq T_{M-I}$, an insulating energy minimum as in Eq. 2 appears and becomes more stable. The stabilization energy defined in eq 3 is $\approx -0.024\text{ ev/Ru}$ at T_{M-I} .

The pressure dependence of the transition may be obtained by adding to Eq. 1 a term $+PdV$ with $dV = \frac{1}{4}(ab\delta c + ac\delta b + bc\delta a)$ with a, b, c the lattice constants of

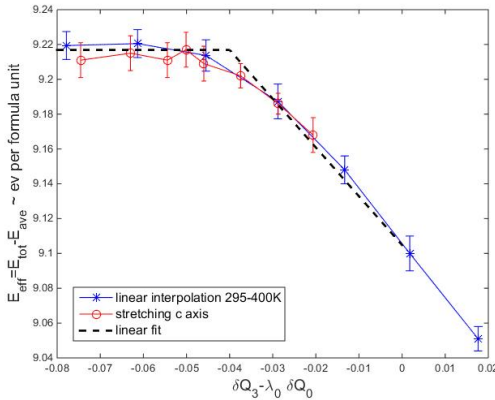


FIG. 2. Effective electron energy of correlated bands $E_{corr} = \langle H_{tot} \rangle - \epsilon_{ave} N_{tot}$ (ϵ_{ave} is the orbitally averaged on-site energy from our MLWF fits to the converged DFT band structure and $N_{tot} = 4$), calculated using DFT+DMFT for a series of structures linearly interpolated between the experimentally observed metallic 400K and insulating 295K structures (solid points, blue on-line) and a series obtained by starting from the insulating structure and stretching the c-axis (open symbols, red on-line) and plotted against a linear combination of octahedral parameters with $\lambda_0 = 0.45$. The dashed line shows a linear fit to the energy $E_{eff} = E_0 - \mathcal{F}_3(\delta Q_3 - \lambda_0 \delta Q_0 - \delta Q_c)\Theta(\delta Q_3 - \lambda_0 \delta Q_0 - \delta Q_c)$ with $\mathcal{F}_3 = 2.8\text{ eV/\AA}$. The error bars are statistical errors from the Monte Carlo solution of the DMFT equations.

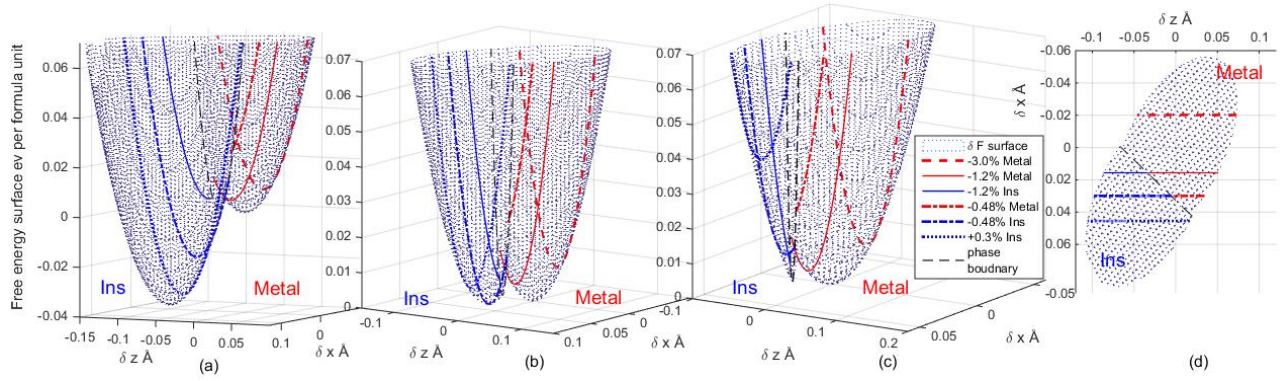


FIG. 3. Free energy surfaces computed for unconstrained bulk Ca_2RuO_4 at temperatures 180 K(a), 350 K(b), and 550 K(c). The metallic and insulating phases are separated by a black dot-dashed line and indicated by labels below the surface. The solid and dashed lines show the one dimensional cuts that the system can explore for films grown under epitaxial strain conditions indicated with the phase indicated by color (blue=insulating, red=metallic). (d) shows the projection of the free energy landscape for $T = 350\text{ K}$ onto the x - z plane.

the Pbca lattice with 4 Ru ions per unit cell. The relation between $\delta a, \delta b, \delta c$ and the change in Ru-O bond length from our relaxation calculation in eq 8 shows that we may write $PdV = P(\beta_3\delta\vec{Q}_3 + \beta_0\delta\vec{Q}_0)$ with $(\beta_3, \beta_0) = (-0.3281, -0.1861)\text{ eV}/(\text{GPa} \cdot \text{\AA})$ per formula unit, so that applied pressure is in effect a linear term shifting the position and value of the energy minimum. The curious fact that hydrostatic pressure increases the Ru-O(2) bond length accounts for the large value of β_3 . From our free energy model we find $P_c = 2.86 - 0.0087T$ (Gpa) which is comparable to $P_c^{\text{exp}} \approx 2.3 - 0.006T$ (Gpa) fitted from published data.²²

We now turn to the metal-insulator transition on epitaxially grown films. In the standard discussion the epitaxial constraint is interpreted as a strain field, to be treated as a Lagrange multiplier analogously to the pressure. However, the tight association of the in-plane lattice parameter and the Ru-O(1) bond length means that in epitaxially grown Ca_2RuO_4 films the epitaxy provides a constraint: instead of freely minimizing Eq. 1 over the full space of structural variables, the system can explore only a one dimensional cut across the energy landscape, meaning that energy minima that are present in the unconstrained case may not be accessible.

The solid and dashed lines in Fig. 3 show the one dimensional cuts that can be explored under different strain conditions. The stable structures for the strained films are the minimum points on these curves; because the curves typically do not pass near the global minima, the phase transition becomes much more expensive. We see that there is only a small range of compressive strain around -1.2% (corresponds to 295K) where a metal-insulator transition occurs in a reasonable temperature range. For a larger compressive strain the system is always a metal while for a tensile or small compressive strain the material is always an insulator. This is consistent with recent experimental observations³⁴ of thin

films of Ca_2RuO_4 grown epitaxially on NdGaO_3 ($+0.3\%$ strain), NSAT (-0.48%), LaAlO_3 (-1.6%) and NdAlO_3 (-3.0%). The films grown on NdGaO_3 and NSAT (tensile or small compressive strain) remained insulating up to 550 K. The film grown on NdAlO_3 (large compressive strain) was metallic down to the lowest temperature in the experiments. The film grown on LaAlO_3 (moderate compressive strain) remained metallic down to $\approx 200\text{ K}$ and then displayed a weak metal-insulator transition.

In summary, we have demonstrated the importance of lattice energetics in the Mott metal-insulator transition. We defined the relevant free energy, computed the lattice stabilization energy, and elucidated the crucial and previously unappreciated role of epitaxial constraints. We focussed on Ca_2RuO_4 , which has two simplifying features: the metal and insulator have the same symmetry (the change in lattice structure is the same in each unit cell) and octahedral rotations are of minor importance, so the order parameter couples linearly to strains and the in-plane Ru-O bond lengths determine the Ru-Ru spacing. Our treatment of the temperature dependence was phenomenological. Providing a less phenomenological treatment of the temperature dependence of the electronic and lattice free energies in Ca_2RuO_4 is an interesting direction for future research. More importantly, a generalization of the theory to cases where octahedral rotations are important (perovskite titanates and vanadates) or the insulating phase breaks a translation symmetry (manganites and nickelates) so that strain couples via nonlinear terms in the elastic theory, is urgently needed.

Acknowledgements: We thank H. Nair, D.Schlom, Jacob Ruf and K.Shen for sharing data in advance of publication and for helpful discussions. The DMFT calculations using codes written by H. T. Dang were performed on the Yeti HPC cluster at Columbia university. This research is supported by the Basic Energy Science Program of the Department of Energy under grant ER-04169 and Cornell Center for Materials Research with funding from the NSF MRSEC program (DMR-1120296).

- ¹ M. Imada, A. Fujimori, and Y. Tokura, *Rev. Mod. Phys.* **70**, 1039 (1998).
- ² M. Cwik, T. Lorenz, J. Baier, R. Müller, G. André, F. Bourée, F. Lichtenberg, A. Freimuth, R. Schmitz, E. Müller-Hartmann, and M. Braden, *Phys. Rev. B* **68**, 060401 (2003).
- ³ E. Pavarini, S. Biermann, A. Poteryaev, A. I. Lichtenstein, A. Georges, and O. K. Andersen, *Phys. Rev. Lett.* **92**, 176403 (2004).
- ⁴ A. J. Millis, P. B. Littlewood, and B. I. Shraiman, *Phys. Rev. Lett.* **74**, 5144 (1995).
- ⁵ A.-M. Haghiri-Gosnet and J. P. Renard, *J. Phys. D: Appl. Phys* **36**, R127?R150 (2003).
- ⁶ Y. Tokura, *Rep. Prog. Phys.* **69**, 797?851 (2006).
- ⁷ J. B. Torrance, P. Lacorre, A. I. Nazzal, E. J. Ansaldo, and C. Niedermayer, *Phys. Rev. B* **45**, 8209 (1992).
- ⁸ J. A. Alonso, J. L. García-Muñoz, M. T. Fernández-Díaz, M. A. G. Aranda, M. J. Martínez-Lope, and M. T. Casais, *Phys. Rev. Lett.* **82**, 3871 (1999).
- ⁹ M. T. Fernández-Díaz, J. A. Alonso, M. J. Martínez-Lope, M. T. Casais, J. L. García-Muñoz, and M. A. G. Aranda, *Physica B* **276**, 218 (2000).
- ¹⁰ M. Medarde, C. Dallera, M. Grioni, B. Delley, F. Vernay, J. Mesot, M. Sikora, J. A. Alonso, and M. J. Martínez-Lope, *Phys. Rev. B* **80**, 245105 (2009).
- ¹¹ N. F. Mott, *Proc. Phys. Soc. A* **62**, 416 (1949).
- ¹² T. Miyake, F. Aryasetiawan, and M. Imada, *Phys. Rev. B* **80**, 155134 (2009).
- ¹³ G. Kotliar, S. Y. Savrasov, K. Haule, V. S. Oudovenko, O. Parcollet, and C. A. Marianetti, *Rev. Mod. Phys.* **78**, 865 (2006).
- ¹⁴ H. Park, A. J. Millis, and C. A. Marianetti, *Phys. Rev. B* **89**, 245133 (2014).
- ¹⁵ I. Leonov, V. I. Anisimov, and D. Vollhardt, *Phys. Rev. Lett.* **112**, 146401 (2014).
- ¹⁶ K. Haule and G. L. Pascut, *Phys. Rev. B* **94**, 195146 (2016).
- ¹⁷ S. Nakatsuji, S. ichi Ikeda, and Y. Maeno, *Journal of the Physical Society of Japan* **66**, 1868 (1997), <http://dx.doi.org/10.1143/JPSJ.66.1868>.
- ¹⁸ M. Braden, G. André, S. Nakatsuji, and Y. Maeno, *Phys. Rev. B* **58**, 847 (1998).
- ¹⁹ O. Friedt, M. Braden, G. André, P. Adelman, S. Nakatsuji, and Y. Maeno, *Phys. Rev. B* **63**, 174432 (2001).
- ²⁰ L. Miao, P. Silwal, X. Zhou, I. Stern, J. Peng, W. Zhang, L. Spinu, Z. Mao, and D. Ho Kim, *Applied Physics Letters* **100**, 052401 (2012), <http://dx.doi.org/10.1063/1.3680250>.
- ²¹ Y. Xin, X. Wang, Z. Zhou, and J. Zheng, *Thin Solid Films* **515**, 3946 (2007).
- ²² F. Nakamura, *Journal of the Physical Society of Japan* **76**, 96 (2007), <https://doi.org/10.1143/JPSJS.76SA.96>.
- ²³ P. Steffens, O. Friedt, P. Alireza, W. G. Marshall, W. Schmidt, F. Nakamura, S. Nakatsuji, Y. Maeno, R. Lengsdorf, M. M. Abd-Elmeguid, and M. Braden, *Phys. Rev. B* **72**, 094104 (2005).
- ²⁴ H. Rho, S. L. Cooper, S. Nakatsuji, H. Fukazawa, and Y. Maeno, *Phys. Rev. B* **71**, 245121 (2005).
- ²⁵ J. H. Jung, Z. Fang, J. P. He, Y. Kaneko, Y. Okimoto, and Y. Tokura, *Phys. Rev. Lett.* **91**, 056403 (2003).
- ²⁶ S.-M. Souliou, J. c. v. Chaloupka, G. Khaliullin, G. Ryu, A. Jain, B. J. Kim, M. Le Tacon, and B. Keimer, *Phys. Rev. Lett.* **119**, 067201 (2017).
- ²⁷ P. B. Allen, H. Berger, O. Chauvet, L. Forro, T. Jarlborg, A. Junod, B. Revaz, and G. Santi, *Phys. Rev. B* **53**, 4393 (1996).
- ²⁸ J. S. Ahn, J. Bak, H. S. Choi, T. W. Noh, J. E. Han, Y. Bang, J. H. Cho, and Q. X. Jia, *Phys. Rev. Lett.* **82**, 5321 (1999).
- ²⁹ E. Gorelov, M. Karolak, T. Wehling, F. Lechermann, A. Lichtenstein, and E. Pavarini, *Physical review letters* **104**, 226401 (2010).
- ³⁰ H. T. Dang, J. Mravlje, A. Georges, and A. J. Millis, *Phys. Rev. B* **91**, 195149 (2015).
- ³¹ Q. Han, H. T. Dang, and A. J. Millis, *Phys. Rev. B* **93**, 155103 (2016).
- ³² D. Sutter, C. Fatuzzo, S. Moser, M. Kim, R. Fittipaldi, A. Vecchione, V. Granata, Y. Sassa, F. Cossalter, G. Gatti, M. Grioni, H. Ronnow, N. Plumb, C. Matt, M. Shi, M. Hoesch, T. Kim, T. Chang, H. Jeng, C. Jozwiak, A. Bostwick, E. Rotenberg, A. Georges, T. Neupert, and C. J., *Nature Communications* **8**, 15176 (2017).
- ³³ M. Kim, J. Mravlje, M. Ferrero, O. Parcollet, and A. Georges, *arXiv:1707.02462* (2017).
- ³⁴ H. Nair, J. Ruf, Y. Liu, N. Shukla, B. Grisafe, C. S. . Chang, Q. Han, A. Millis, D. A. Muller, S. Datta, K. Shen, and D. G. Schlom, *EMA-S2-032* (2017).
- ³⁵ G. Kresse and J. Hafner, *Phys. Rev. B* **47**, 558 (1993).
- ³⁶ G. Kresse and J. Furthmüller, *Comput. Mat. Sci.* **6**, 15 (1996).
- ³⁷ G. Kresse and J. Furthmüller, *Phys. Rev. B* **54**, 11169 (1996).
- ³⁸ G. Kresse and D. Joubert, *Phys. Rev. B* **59**, 1758 (1999).
- ³⁹ H. T. Dang and A. J. Millis, *Phys. Rev. B* **87**, 155127 (2013).
- ⁴⁰ N. Marzari and D. Vanderbilt, *Phys. Rev. B* **56**, 12847 (1997).
- ⁴¹ I. Souza, N. Marzari, and D. Vanderbilt, *Phys. Rev. B* **65**, 035109 (2001).
- ⁴² O. Parcollet, M. Ferrero, T. Ayral, H. Hafermann, I. Krivenko, L. Messio, and P. Seth, *Computer Physics Communications* **196**, 398 (2015).
- ⁴³ P. Seth, I. Krivenko, M. Ferrero, and O. Parcollet, *Computer Physics Communications* **200**, 274 (2016).

Supplementary Information

I. DFT CALCULATIONS

DFT and DFT+U calculations were performed using the spin-polarized Generalized Gradient Approximation and Local (Spin) Density Approximation as implemented in VASP^{35–38}, with energy cutoff 600 eV and K mesh $8 \times 8 \times 4$ which has been compared with smaller K meshes to prove convergence. Structures were relaxed using the conjugate-gradient algorithm implemented in VASP. The convergence criterion of the electronic self-consistent loop is the total energy change and the band structure energy change smaller than 10^{-7} eV/unit cell, and the convergence of ionic relaxation loop is controlled by all forces smaller than 0.001 eV/Å.

II. STRUCTURAL RELAXATION: RELEVANCE OF OCTAHEDRAL ROTATIONS AND TILTS

To investigate the importance of octahedral rotations and tilts we performed DFT calculations where we fixed in-plane Ru-Ru distance as a series of values from 4.0 Å to 3.8 Å and relaxed the internal coordinates and c lattice constant. We used GGA as a representative of the metallic phase and GGA+U as a representative of the insulating phase. In the GGA plus U calculations a ferromagnetic ground state was assumed and the parameters $U = 3.0$ eV and $J = 0.6$ eV were used; these choices yield an orbital occupancy $n_{xy} = 2$, $n_{xz/yz} = 1$ and a band gap ~ 0.3 eV similar to that predicted by our DMFT calculations for the insulating phase.

The Fig. 4 present results in terms of rotation angles ϕ , θ and Θ . ϕ is the rotation of a RuO_6 octahedron about the z axis (the two different Ru in the same plane of a given unit cell have rotations of equal magnitude and opposite sign). θ is the angle between the Ru-O(2) bond and the z direction (normal to the Ru-O plane). Finally, we define Θ as the magnitude of the angle between the Ru-O(1) bond and the in-plane Ru-Ru bond, so the relation between the Ru-O(1) bond length and the in-plane lattice constants is

$$d_{\text{Ru-O}(1)} = \frac{\sqrt{a^2 + b^2}}{4\cos\Theta} \quad (6)$$

We see that the bond angles are very similar for the DFT and DFT+U calculations and change only slightly as the Ru-Ru distance is varies across the relevant range. In particular the crucial parameter Θ that relates the Ru-O(1) bond length to the Ru-Ru distance has no noticeable change. This shows that the in-plane strains are absorbed by changes in the Ru-O(1) bond length and not by octahedral rotations.

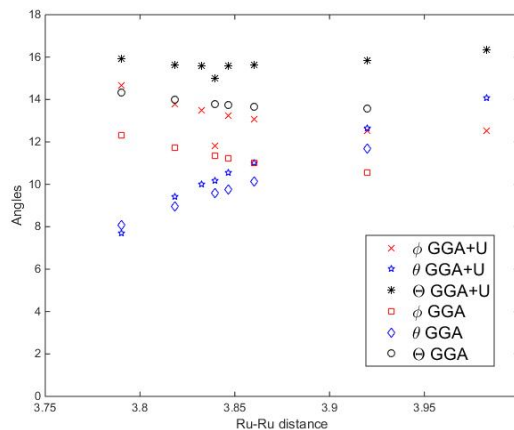


FIG. 4. Rotation angles plotted against in-plane nearest neighbor Ru-Ru distance computed by enforcing fixed in-plane nearest neighbor Ru-Ru distance and fully relaxing remaining coordinates using GGA (square, diamond, circle points) and GGA+U (cross, star, pentagram points).

III. ESTIMATION OF STIFFNESS PARAMETERS K

The K matrix defined in the main text is in essence the energy cost of changes in the Ru-O(2) and mean Ru-O(1) bond lengths after relaxation of the other structural degrees of freedom. Here we present LSDA+U results obtained by varying lattice parameters in the Pbc symmetry and relaxing the inner coordinates. LSDA is chosen because it provides a pressure dependence more comparable to the experiments. By fitting the results of many DFT calculations and expressing the fit in terms of in-plane equal distortion $\delta s = \frac{1}{\sqrt{2}}(\delta a + \delta b)$, out of plane bond length δc , and in-plane shear $\delta Q_1 = \frac{1}{\sqrt{2}}(\delta a - \delta b)$, we find

$$\delta E \sim \frac{1}{2} \begin{pmatrix} \delta s & \delta c & \delta Q_1 \end{pmatrix} \mathbf{W} \begin{pmatrix} \delta s \\ \delta c \\ \delta Q_1 \end{pmatrix} = \frac{1}{2} \begin{pmatrix} \delta s & \delta c & \delta Q_1 \end{pmatrix} \begin{pmatrix} 5.15 & 1.59 & -0.16 \\ 1.59 & 1.05 & 0.015 \\ -0.16 & 0.015 & 0.72 \end{pmatrix} \begin{pmatrix} \delta s \\ \delta c \\ \delta Q_1 \end{pmatrix} \quad (7)$$

Also from the DFT calculations we found that the relation between changes in Ru-O bond lengths $\delta x, \delta y, \delta z$ and changes in lattice parameters $\delta a, \delta b, \delta c$ and Ru-O(1) and Ru-O(2) bond lengths is approximately linear as expected from the results of the previous section.

$$\begin{pmatrix} \delta x \\ \delta y \\ \delta z \end{pmatrix} = dB \begin{pmatrix} \delta a \\ \delta b \\ \delta c \end{pmatrix} = \begin{pmatrix} 0.1472 & 0.2186 & -0.0079 \\ 0.1570 & 0.2253 & 0.0004 \\ -0.0144 & -0.0587 & 0.0746 \end{pmatrix} \begin{pmatrix} \delta a \\ \delta b \\ \delta c \end{pmatrix} \quad (8)$$

A better way to understand the relation between octahedral distortions and the lattice constants distortions is to express the matrix dB in basis of $\delta s^o = \frac{1}{\sqrt{2}}(\delta x + \delta y)$, $\delta Q_1^o = \frac{1}{\sqrt{2}}(\delta x - \delta y)$ and δz and the corresponding basis of δs , δQ_1 and δc of lattice constants distortions.

$$\begin{pmatrix} \delta s^o \\ \delta z \\ \delta Q_1^o \end{pmatrix} = dB \begin{pmatrix} \delta s \\ \delta c \\ \delta Q_1 \end{pmatrix} = \begin{pmatrix} 0.3740 & -0.0053 & -0.0698 \\ -0.0517 & 0.0746 & 0.0313 \\ -0.0082 & -0.0059 & -0.0015 \end{pmatrix} \begin{pmatrix} \delta s \\ \delta c \\ \delta Q_1 \end{pmatrix} \quad (9)$$

From eq 7 we see that δQ_1 is essentially decoupled from the other variables; we ignore it henceforth. Then the in-plane distortion shows $\delta s^o \approx \frac{1}{2\sqrt{2}}\delta s$ which proves the relation between $\delta x, \delta y$ and $\delta a, \delta b$ is essentially given by geometry as seen in the previous section. The in-plane Ru-O(1) bonds barely depends on the change in apical lattice constant parameter, however the apical Ru-O(2) bond length couples to both the change in the c axis lattice parameter and in-plane distortion δs .

We now write a general expression for the energy as a functional of $\delta s, \delta c$ and δz ,

$$E = \frac{1}{2} \begin{pmatrix} \delta s & \delta c & \delta z \end{pmatrix} \begin{pmatrix} C_{11} & C_{12} & -b_1 K_{zz} \\ C_{12} & C_{22} & -b_2 K_{zz} \\ -b_1 K_{zz} & -b_2 K_{zz} & K_{zz} \end{pmatrix} \begin{pmatrix} \delta s \\ \delta c \\ \delta z \end{pmatrix} \quad (10)$$

. Minimizing eq 10 over δz gives the DFT relaxation energy in eq 7 (with δQ_1 neglected); minimizing eq 10 over δc gives the energy form we need. The off diagonal terms $C_{13} = -b_1 K_{zz}$ and $C_{23} = -b_2 K_{zz}$ are due to the approximate relation between apical bond distortion and lattice constants distortions: if we fix the lattice parameters variables δs and δc and minimize δz , we got

$$\delta z \approx -\frac{C_{13}}{K_{zz}} \delta s - \frac{C_{23}}{K_{zz}} \delta c = b_1 \delta s + b_2 \delta c \quad (11)$$

The minimized energy has a form:

$$\delta E(s, c) = \frac{1}{2} \begin{pmatrix} \delta s & \delta c \end{pmatrix} \begin{pmatrix} C_{11} - b_1^2 K_{zz} & C_{12} - b_1 b_2 K_{zz} \\ C_{12} - b_1 b_2 K_{zz} & C_{22} - b_2^2 K_{zz} \end{pmatrix} \begin{pmatrix} \delta s \\ \delta c \end{pmatrix} \quad (12)$$

$\delta E(s, c)$ may be compared directly to eq 7 So we identify (unit $ev/\text{\AA}^2$ per formula unit)

$$C_{11} = W_{11} + b_1^2 K_{zz} = 5.27; \quad C_{12} = b_1 b_2 K_{zz} + W_{12} = 1.43; \quad C_{22} = b_2^2 K_{zz} + W_{22} = 1.29; \quad (13)$$

Fixing δs and δz and minimizing over δc gives

$$\delta E(s, z) = \frac{1}{2}(\delta s, \delta z) \left(\begin{pmatrix} C_{11} & -b_1 K_{zz} \\ -b_1 K_{zz} & K_{zz} \end{pmatrix} - \frac{1}{C_{22}} \begin{pmatrix} C_{12}^2 & -C_{12} b_2 K_{zz} \\ -C_{12} b_2 K_{zz} & b_2^2 K_{zz}^2 \end{pmatrix} \right) \begin{pmatrix} \delta s \\ \delta z \end{pmatrix} \quad (14)$$

We require an estimation for K_{zz} which may be obtained by using the Raman apical oxygen phonon frequency from Ref^{24,25} which is about $600 \text{ cm}^{-1} \approx 0.075 \text{ eV}$. This phonon has 2 oxygen ions moving against an essentially immobile (because much heavier) Ru, so

$$K_{zz} = 2K_{\text{Ru-O}(2)} = 2\omega_{ph}^2 M_O \approx 42 \text{ eV}/\text{\AA}^2 \quad (15)$$

since the change in the octahedron involves two bonds (plus and minus z).

Putting all these numbers in to Eq. 14 and changing to the basis of octahedral distortions, using $\delta s^o \approx \frac{1}{2\sqrt{2}}\delta s$, gives (in units of $\text{eV}/\text{\AA}^{-2}$):

$$\delta E(s^o, z) = \frac{1}{2} \begin{pmatrix} \delta s^o & \delta z \end{pmatrix} \begin{pmatrix} 29.47 & 15.97 \\ 15.97 & 34.37 \end{pmatrix} \begin{pmatrix} \delta s^o \\ \delta z \end{pmatrix} \quad (16)$$

Finally, we can make contact with our previous formalism by using eq 4

$$\delta E(\delta Q_3, \delta Q_0) = \frac{1}{2} \begin{pmatrix} \delta Q_3 & \delta Q_0 \end{pmatrix} \begin{pmatrix} 17.69 & 7.63 \\ 7.63 & 46.16 \end{pmatrix} \begin{pmatrix} \delta Q_3 \\ \delta Q_0 \end{pmatrix} \quad (17)$$

This is the effective stiffness matrix \mathbf{K} we would use in the quadratic form lattice energy in main text Eq. 1.

IV. DFT+DMFT CALCULATIONS

We solve the correlation problem following previous work on related compounds^{30,31,39}. For a given lattice structure we used the non-spin-polarized Generalized Gradient Approximation as implemented in VASP to calculate the electronic structure. The calculation is on 11 by 11 by 7 k-mesh with energy cutoff 500 eV. We can afford the larger K mesh because DFT is less computationally demanding than DFT+U. Then, we extracted the near Fermi surface t_{2g} derived bands via a fit to maximally localized Wannier Functions (MLWF) by wannier90^{40,41}. Figure 5 shows as examples the calculated band structures and MLWF fits for the experimentally observed 400K (metallic) and 295K (insulating) structures.

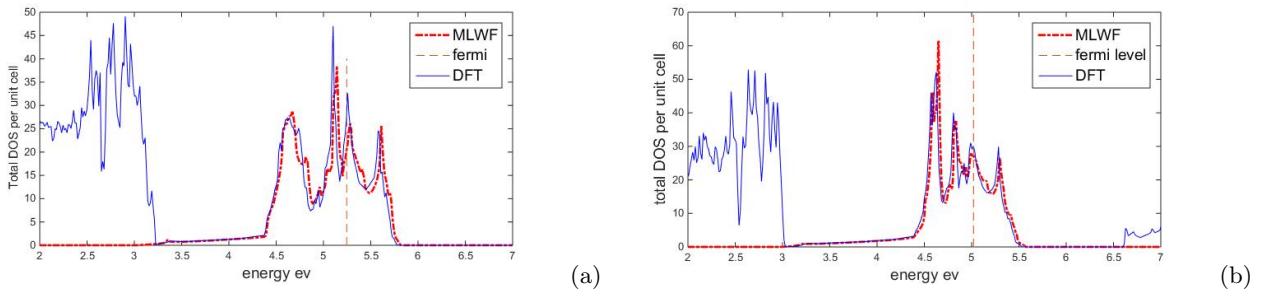


FIG. 5. Density of states calculated using the VASP implementation of the GGA for the experimentally observed 400K (left panel) and 295K (right panel) structures^{18,19}. Blue solid lines represent DFT calculations and red dashed lines represent the MLWF fit. Black dashed lines indicate the Fermi level.

The projection of the DFT Hamiltonian onto the Wannier basis describing the t_{2g} manifold along with fully rotationally invariant Slater-Kanamori interactions specified by the interaction parameters $U = 2.3 \text{ eV}$ and $J = 0.35 \text{ eV}$ defines a multiorbital Hubbard model^{31,39} which we solve in the single-site DMFT approximation using the hybridization expansion variant of the continuous-time quantum Monte Carlo (CT-HYB) solver as implemented in the Toolbox for Research on Interacting Quantum Systems (TRIQS) library^{42,43}. (Note that the 4 Ru ions of the experimental Pbca structure are equivalent up to a rotation to align the coordinate axes to the local octahedral axes).

We compute the energy of the correlated electrons from the standard formula

$$E_{corr} = N \sum_{\alpha\sigma} \frac{1}{\beta} \sum_n (i\omega_n \cdot G_{\alpha\sigma}^{loc}(\omega_n) - \frac{1}{2} \Sigma_{\alpha\sigma}(\omega_n) G_{\alpha\sigma}^{loc}(\omega_n)) e^{i\omega_n \delta} + \mu N \quad (18)$$

where $G_{\alpha\sigma}^{loc}$ is the on site Green function for orbital α emerging from the converged DMFT solution. To control the formally divergent behavior at high frequencies we added and subtracted the known high frequency asymptotics, writing

$$E_{corr} = \sum_{\alpha\sigma} \left\{ \frac{1}{\beta} \sum_n \left(G^{\alpha\sigma} - \frac{1}{i\omega_n} - \frac{G_2^{\alpha\sigma}}{(i\omega_n)^2} \right) i\omega_n + \frac{G_2^{\alpha\sigma}}{2} - \frac{1}{2\beta} \sum_n (\Sigma^{\alpha\sigma} - \Sigma_0^{\alpha\sigma}) G^{\alpha\sigma}(i\omega_n) - \frac{1}{2} \Sigma_0^{\alpha\sigma} n^{\alpha\sigma} \right\} + \mu N_{tot} \quad (19)$$

Σ_0 is the Hartree contribution to the self energy, which we compute with the Slater-Kanamori interaction and the occupancies of the converged solutions and G_2 involves both Σ_0 and the high frequency limit of the hybridization function (obtained from the MLWF fits) and $N_{tot} = 4$ per Ru atom in Ca_2RuO_4 .

The energy depends on the ionic positions via band parameters (hoppings and on-site energies) obtained from the MLWF fits. We define the average energy parameter

$$\epsilon_{ave} = \frac{1}{2}(\epsilon_{xy}^0 + \epsilon_{\perp}^0) = \frac{1}{2}(\epsilon_{xy}^0 + \frac{\epsilon_{yz}^0 + \epsilon_{zx}^0}{2}) \quad (20)$$

It has the same dependence on distortion in both insulator and metal phase, because ϵ_{ave} is calculated on DFT level. Since the force term \vec{F} only depends on the difference of derivative of energy with respect to $\delta\vec{Q}$ between insulating phase and metallic phase, we absorb ϵ_{ave} into the chemical potential by plotting $E_{corr} - \epsilon_{ave}N_{tot}$ as in fig 2 and fitting

$$E_{eff} = E_{corr} - \epsilon_{ave}N_{tot} = E_0 - (\mathcal{F}_3\delta Q_3 + \mathcal{F}_0\delta Q_0 - \mathcal{F}_3\delta Q_c)\Theta(\delta Q_3 - \lambda_0\delta Q_0 - \delta Q_c) \quad (21)$$

to get the the force term parameters $\vec{F} = (\mathcal{F}_3, \mathcal{F}_0) = \mathcal{F}_3(1, -\lambda_0)$.

Main text fig 2 shows that the linear fit is good except in the vicinity of the transition where some rounding is evident. It may be understood by looking at the orbital polarizations $\delta n = \frac{1}{2}(n_{xy} - (n_{yz} + n_{zx}))$ on these structures vs level splitting $\Delta = \frac{\epsilon_{yz}^0 + \epsilon_{xy}^0}{2} - \epsilon_{xy}^0$ shown in fig 6. The orbital polarization shows an upturn near the critical orbital splitting ($\Delta_c \sim 0.2$ eV for interpolated structures and $\Delta_c \sim 0.16$ eV for stretching c axis structures). Whether the transition is first order or second order with vary rapid variation near the critical point, it does not influence $\delta\vec{Q}$ as in eq 2.

We finally estimate the second order derivatives of F with respect to δQ . If we look at the occupancy away from the phase boundary, it shows a linear relation with Δ . Using eq 20 we write

$$E_{band} = \epsilon_{xy}^0 n_{xy} + \epsilon_{yz}^0 n_{yz} + \epsilon_{zx}^0 n_{zx} = \epsilon_{ave}N_{tot} - \Delta \frac{1}{2}(n_{xy} - (n_{yz} + n_{zx})) \quad (22)$$

Thus

$$\frac{\partial E_{corr}}{\partial \Delta} \sim \delta n = \frac{1}{2}(n_{xy} - n_{yz} - n_{zx}) \quad (23)$$

Therefore

$$\frac{\partial^2 E_{corr}}{\partial \Delta^2} \sim -\frac{\partial \delta n}{\partial \Delta} \quad (24)$$

From fig 6, we used the stretched c axis protocol (red circles) to eliminate the band width effect. From $\delta n = \frac{1}{2}(n_{xy} - (n_{yz} + n_{zx})) = \chi\Delta$, If we fit the three points in insulating phase and the last three points in metal phase separately (black dashed lines), we get $\frac{\partial^2 E_{corr}^I}{\partial \Delta^2} \approx 2.2$ eV⁻¹ and $\frac{\partial^2 E_{corr}^M}{\partial \Delta^2} \approx 3.2$ eV⁻¹. By fitting the relation between orbital spacing and octahedral distortion we get $\Delta \approx -1.84\delta Q_3$. Thus the second order correction to the free energy can be neglected since $\delta K^{ins} - \delta K^{metal} \approx 3.4\text{eV}/\text{\AA}^2$ which is much smaller compared with eigenvalues of lattice stiffness \mathbf{K} . So we still use the linear model in eq 21 to approximate the effective energy.

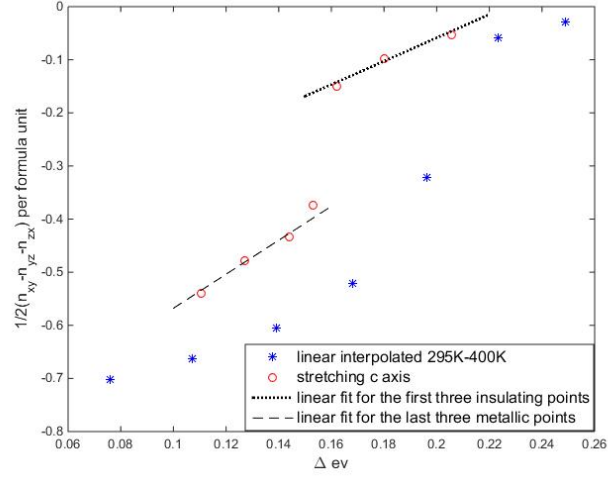


FIG. 6. Orbital polarization vs orbital splitting $\Delta = \frac{\epsilon_{yz}^0 + \epsilon_{xy}^0}{2} - \epsilon_{xy}^0$ from DFT+MLWF calculation for linear interpolated structures (red circle) from 295 K experiment measured atom positions to 400K atom positions and stretching c axis (blue star points) structures with in-plane lattice constants $a = b = 5.44 \text{ \AA}$. Dashed lines are linear fit to get $\frac{d\delta n}{d\Delta}$